

HORIZON-CL5-2022-D3-01-11

Demonstration of innovative forms of storage and their successful operation and integration into innovative energy system and grid architectures



AGISTIN

Advanced Grid Interfaces for
innovative STorage INtegration

D3.2 Open-source simulation models of the pertinent grid coupling systems open for parametrisation according to individual load, generation, and storage technologies

Document properties

FUNDING PROGRAM	HORIZON EUROPE
GRANT AGREEMENT NUMBER	101096197
PROJECT	AGISTIN
DELIVERABLE ID	D3.2
TITLE	Open-source simulation models of the pertinent grid coupling systems open for parametrisation according to individual load, generation, and storage technologies
DISTRIBUTION LEVEL	PU
DUE DATE	30-06-2025
DATE SUBMITTED	30-06-2025
VERSION	V1
WORK PACKAGE	WP3
LEAD PARTICIPANT	University of Kassel
TOTAL NUMBER OF PAGES	36



All intellectual property rights are owned by the AGISTIN consortium members and are protected by the applicable laws. Except where otherwise specified, all document contents are: “© AGISTIN project - All rights reserved”. Reproduction is not authorised without prior written agreement. The commercial use of any information contained in this document may require a license from the owner of that information.

All AGISTIN consortium members are also committed to publish accurate and up to date information and take the greatest care to do so. However, the AGISTIN consortium members cannot accept liability for any inaccuracies or omissions, nor do they accept liability for any direct, indirect, special, consequential, or other losses or damages of any kind arising out of the use of this information.

Views and opinion stated in this report reflects the opinion of the authors and not the opinion of the European Commission. The European Union is not liable for any use that may be made of the information contained in this document.

Version history

VERSION	DATE	COMMENT
V0.1	20-04-2025	FIRST DRAFT
V0.2	20-06-2025	FIRST REVIEW
V1	30-06-2025	FINAL VERSION





Executive Summary

AGISTIN, a Horizon Europe project spanning from 2023 to 2026, focused on empowering industrial grid stakeholders to swiftly implement energy efficiency solutions via advanced communication infrastructure. This will be achieved through the integration of renewables, innovative energy storage technologies, hybrid AC/DC coupling, variable frequency drivers, electric vehicle (EV) chargers, etc.

This deliverable shows the open-source simulation models of the pertinent grid coupling systems open for parameterisation according to individual load, generation and storage technologies.

To show the effectiveness and the benefits of an Advanced Grid Interface (AGI), dynamic models of the units and the complete AGI are needed. The unit models can be parameterized to represent different use cases.

First, this report presents the dynamic unit models for use in MATLAB/Simulink. Different loads like an electrolyzer or a hydro pump are presented. The descriptions contain the modeling approach, the used equations and parameters. Also, grid following and grid-forming models are shown. The grid-forming models have specific features like overcurrent limitation and asymmetric inertia provision. For all components made by AGISTIN consortium members, simulation results are given. These results show the dynamic behaviour of the model and can be used as a reference in further use of the models. For clarification of the feature asymmetric inertia, it is shown in a 3 inverter system.

Furthermore, a DC-coupled and an AC-AGI are shown. The latter represents the use case of the hydrogen production facility of SHELL.

The models are publicly available in GitHub under https://github.com/AGISTIN-Project/AGISTIN_Project. The models will see further development during the project and will serve as a basis for benchmarking in T3.6.

Contents

1	Introduction	7
2	Models	8
2.1	Alkaline electrolyzer	8
2.2	Supercapacitor	13
2.3	Lithium-Ion Battery	15
2.4	Hydro Pump	17
2.5	PV	20
2.6	Capacitor	20
2.7	Grid-Following Inverter	20
2.8	Grid-Forming Inverter	20
2.9	Grid-Forming Inverter for Tailored Inertia	21
2.9.1	General Augmentation of the Grid Model: Frequency Measurement	21
2.9.2	General Augmentations of the Generic Converter Model	23
3	Systems	34
3.1	DC AGI	34
3.2	AC AGI	34
	Bibliography	35

List of Figures

2.1	Equivalent circuit model (ECM) of alkaline electrolysis (AEL) (own representation based on [17])	8
2.2	IV-curve of one cell from values of Table 2.1	9
2.3	Influence for current and voltage for alkaline electrolyzer nominal power.	10
2.4	Design parameters for the 1.5 MW alkaline electrolysis (AEL).	11
2.5	Dynamic operation of the 1500 kW stack	12
2.6	Equivalent circuit model (ECM) of a supercapacitor	13
2.7	Mask with design parameters for the supercapacitor	14
2.8	Dynamic operation of the 1.5 MW supercapacitor	14
2.9	Equivalent circuit model (ECM) of a Lithium-ion battery (LIB) (own representation based on [26])	15
2.10	Mask with design parameters for the 1.5 MW Lithium-ion battery (LIB)	16
2.11	Dynamic operation of the 1.5 MW Lithium-ion battery (LIB)	17
2.12	Operating region of a variable speed pump.	18
2.13	Dynamic model of the hydro pump	18
2.14	Dynamic operation of the hydro pump (Flow)	19
2.15	Dynamic operation of the hydro pump (Pressure)	19
2.16	GFM control structure	20
2.17	RoCoF event with 0.5 Hz/s and inertia response	21
2.18	Grid section for investigation of tailored inertia	22
2.19	Frequency measurement including filtering.	22
2.20	Fast voltage regulator.	24
2.21	Subsystem CurrentControl.	25
2.22	Subsystem for additional inertia in case of active LFSM-O/U.	28
2.23	Subsystem for reduced inertia for fast return from extreme frequencies.	29
2.24	Subsystem for compensation of f forerun caused by feedforward damping.	31
3.1	DC AGI [6].	34
3.2	AC AGI - use case of one project partner	34

List of Tables

2.1	Adjustable parameters of the generic alkaline electrolyzer model with default parameters from [17].	9
2.2	Parameters of a 1.5 MW supercapacitor.	15
2.3	Parameters of a 160 kW hydro pump.	19



Acronyms

2RC second-order Thevenin model

AEL alkaline electrolysis

AGI Advanced Grid Interface

AGISTIN Advanced Grid Interfaces for innovative STorage INtegration

ECM Equivalent circuit model

HER hydrogen evolution reaction

LIB Lithium-ion battery

OER oxygen evolution reaction

PEM proton exchange membrane

SOC state of charge



1 Introduction

The AGISTIN project represents an ambitious endeavour at the intersection of innovative energy storage, renewable technologies, demand response, and grid integration. With its focus on advanced grid-integrated technologies, AGISTIN seeks to pave the way for a more sustainable and efficient energy future. In this comprehensive report, we delve into the project's objectives, selected study cases, and the various challenges and opportunities it encounters.

AGISTIN, aims to demonstrate the feasibility of integrated energy systems combining a variety of technologies, such as renewable energy sources, electric vehicle chargers, and industrial loads, by means of advanced grid infrastructure and hybrid AC/DC coupling. By doing so, AGISTIN aspires to showcase how these integrated systems can deliver cost savings, improved energy efficiency, and reduced environmental impacts.

This documents report the modeling activities in WP 3.3. Models are needed to analyze the benefits and effectiveness of an AGI. With the help of dynamic simulations, it can be shown which system services are offered by the AGI. With the help of the models of individual units the effect of the provision of system services can be analyzed. In this report, the individual unit models like electrolyzer and battery are presented. We show the modeling approach and the parameterization. These parameters can also be changed to trim the model for another use case. The unit models are tested and the simulation results are shown. Also grid-forming controls are included with features like overcurrent protection and asymmetric inertia provision. For clarification of the feature asymmetric inertia, it is shown in a 3 inverter system. The report also shows two AGIs, a DC-coupled AGI and an AC-coupled AGI. Individual unit models are combined in the AGIs, which offer system services like inertia. The AC-AGI represents the use case of SHELL and its hydrogen production facility. More details are given in deliverable D2.1. The two AGIs can be used as a basis for the further development of customized AGIs. Other unit models can be included and the parameters can be adjusted according to the individual's needs. These published models will serve as the base for the benchmarking in T3.6. The AGIs and further improved ones will be tested concerning system services and ranked according to their contribution. During the project, the repository will be maintained and updated. The repository can be found under **https://github.com/AGISTIN-Project/AGISTIN_Project**.

2 Models

This chapter shows and describes the different unit models which are included for modeling purposes.

2.1 Alkaline electrolyzer

The generic alkaline electrolysis (AEL) model is based on an Equivalent circuit model (ECM) structure from [17]. In our case we have variable resistors and constant capacitors, as displayed in Figure 2.1.

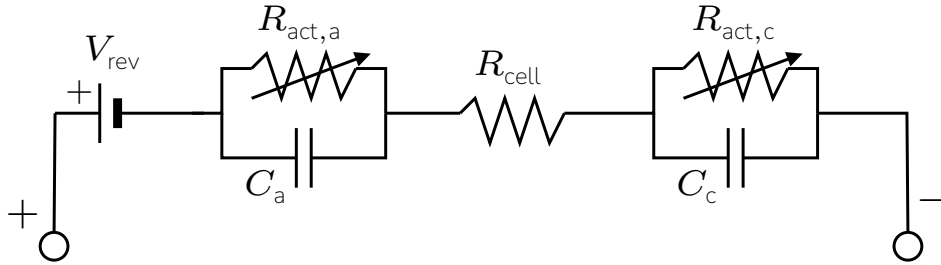


Figure 2.1: ECM of AEL (own representation based on [17])

The resistance of the anode $R_{act,a}$ and cathode $R_{act,c}$ are current dependent and based on the Tafel equation, and therefore calculated by

$$R_{act,a} = \frac{a \log\left(\frac{i}{i_0}\right)}{I}, R_{act,c} = \frac{c \log\left(\frac{i}{i_0}\right)}{I}, \quad (2.1)$$

with the Tafel-slopes a and c , exchange current density i_0 , current density i and total cell current I . The total static electrolyzer voltage V_{ely} is calculated by

$$V_{ely} = N_{cell} (V_{rev} + I (R_{act,a} + R_{act,c} + R_{cell})), \quad (2.2)$$

with the reversible cell voltage V_{res} and number of cells N_{cell} in one stack. The electric dynamic behaviour of the cells is caused by the cathodes and anodes double layer capacities C_a and C_c of the RC-elements. We can consider for the total capacity of the stack a series connection of the capacitors, resulting in

$$C_{a,stack} = \frac{C_a}{N_{cells}}, C_{c,stack} = \frac{C_c}{N_{cells}}. \quad (2.3)$$

The parametrization of the model above with the values in Table 2.1 with the given ranges of the cell active surface area A and number of cells, results in the power and current-voltage behaviour of Figure 2.3. The idea of the scaling is to assume the IV-curve in Figure 2.2 is independent of stack size and the number of cells.

Usually, we would expect the the Tafel slope of the anode to be larger than of the cathode, due to slower reaction kinetics and higher overpotential of oxygen evolution reaction (OER) than of hydrogen evolution reaction (HER). To stay consistent, the parameters of are still implemented as stated in Table 2.1, which are generated by a parameter fit in [17]. Nevertheless, the generic model structure allows the

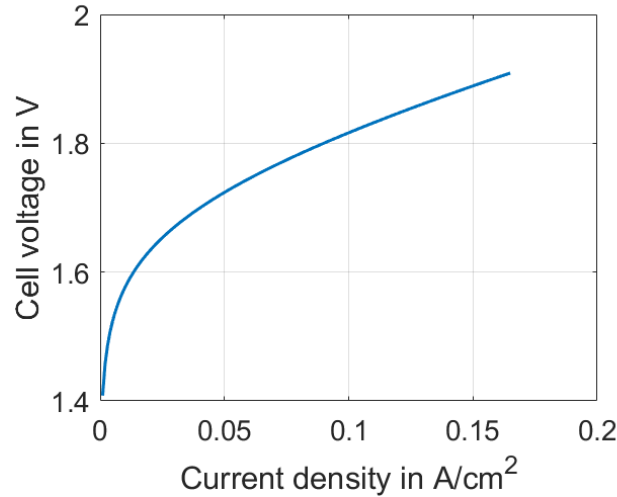


Figure 2.2: IV-curve of one cell from values of Table 2.1

Table 2.1: Adjustable parameters of the generic alkaline electrolyzer model with default parameters from [17].

Parameter	Symbol	Value
Cell active area	A	3000 cm ² to 20 000 cm ²
Number of cells	N_{cell}	100 to 650
Nominal current density	i_{nom}	0.165 A cm ⁻²
Ohmic cell resistance	R_{ohm}	0.89 Ω
Anode cell capacity	C_a	1 mF cm ⁻²
Cathode cell capacity	C_c	100 mF cm ⁻²
Anode Tafel slope	a	0.04 V dec ⁻¹
Cathode Tafel slope	c	0.12 V dec ⁻¹
Exchange current density in	i_0	$1.2 \cdot 10^{-4}$ A cm ⁻²
Reversible cell voltage	V_{rev}	1.26 V

user to replace the parameters in the model mask, displayed in Figure 2.4b. In this model, the operation temperature T and pressure p do not influence the model performance, since we are assuring steady state for the model parameters. This is due to sluggish process time constants in comparison to the eclectic dynamic behaviour.

From the data in Figure 2.3, a two dimensional plot can be extracted for the design nominal voltage of 1500 kW nominal stack load. The curves in Figure 2.4a show the relationship of the stack voltage, or number of cells, to the possible cell active area, which is directly proportional to the current. We can observe that for a fixed nominal power, there is a nonlinear relation of needed cells to the chosen cell surface. In this study, the voltage should be in the range of 700 V to 1200 V. The design parameter of A is set to 10 000 cm², which is in the range of other AEL applications [7]. From this design we get $N_{\text{cell}} = 477$, which can be entered in the model mask, displayed in Figure 2.4b. By pressing the button "Get: power / voltage / current" in the mask, marked in blue, all nominal power, current, and voltage are calculated. Also, there is an option to implement the power range. This has no direct influence on the model and is only used to calculate the power range. The initial conditions for the are marked orange in Figure 2.4b and would need to be set by the user.

The dynamic operation of the model is displayed in Figure 2.5.

There is even less data available in literature for proton exchange membrane (PEM) electrolyzers than for AEL, which might be because of the technologies novelty, compared to the well established AEL. Therefore, in this work we focus on AEL only.

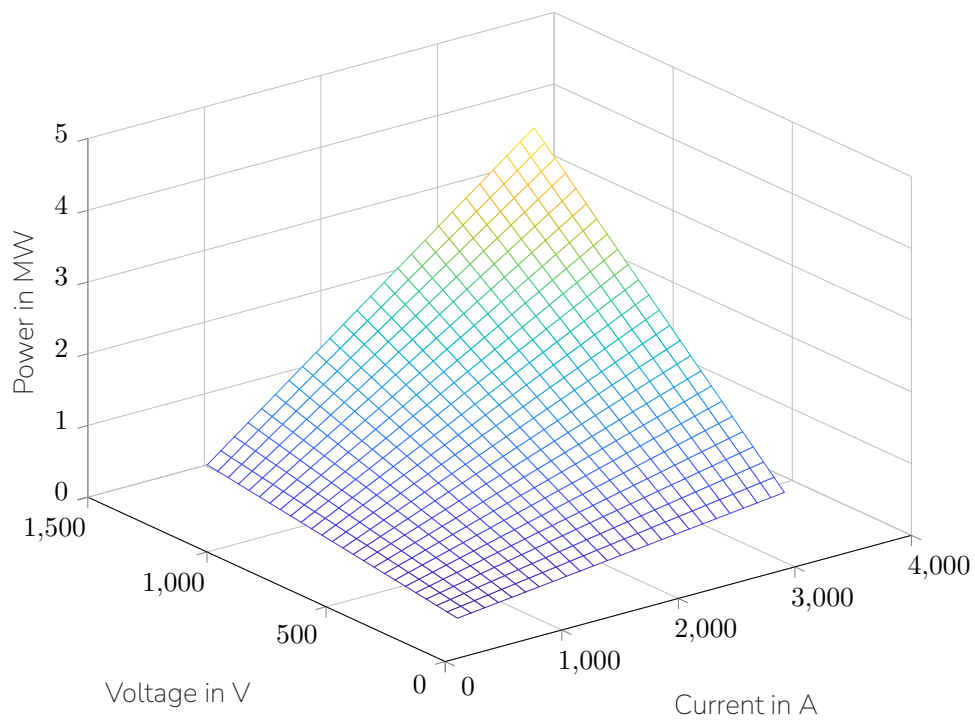
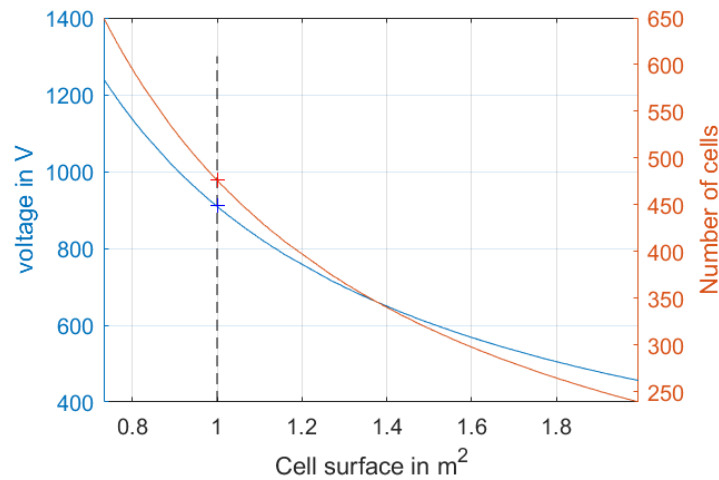
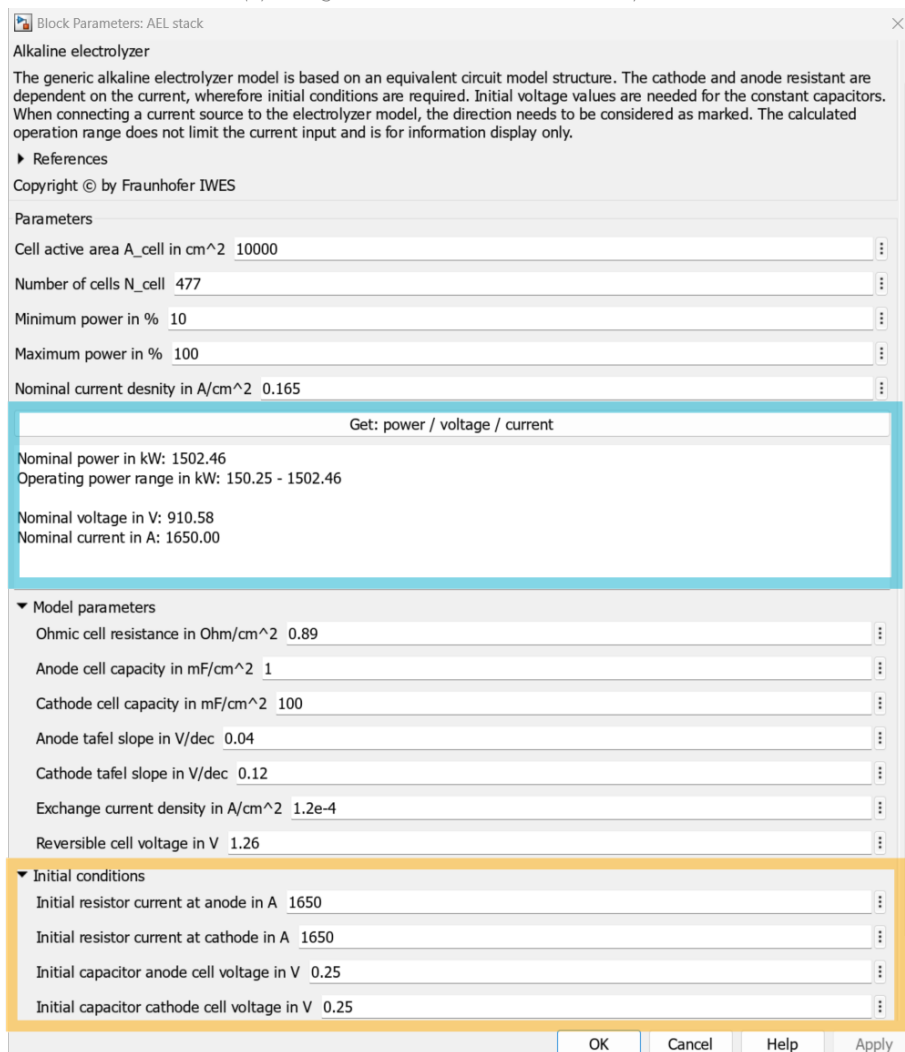


Figure 2.3: Influence for current and voltage for alkaline electrolyzer nominal power.



(a) Design curve for 1500 kW electrolyzer.



(b) Mask of generic model with resulting setting.

Figure 2.4: Design parameters for the 1.5 MW AEL.

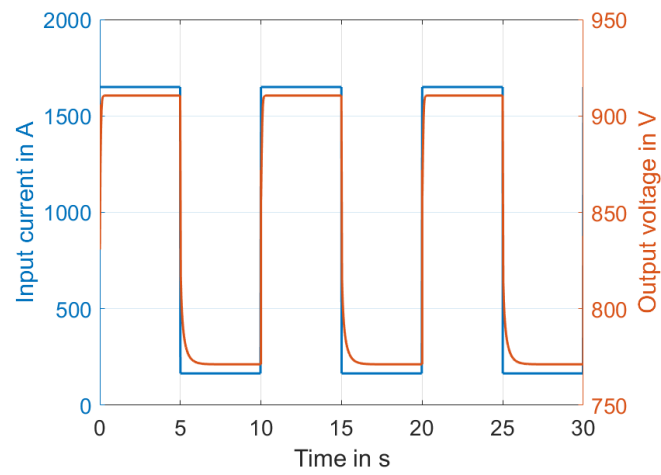


Figure 2.5: Dynamic operation of the 1500 kW stack

2.2 Supercapacitor

Supercapacitor modeling encompasses various approaches, including circuit-oriented, electrochemical, black box, fractional order, porous electrode, impedance, self-discharge, and thermal models. Among these, circuit-oriented models vary in complexity. The Simple RC Model reflects instant dynamic response but lacks detail on complex operational principles, limiting its use to energy storage applications. In contrast, the Series-Parallel RC Model enhances the simple RC model by accounting for leakage currents through the parallel resistance, making it suitable for grid-level applications, which is why it was chosen as a generic supercapacitor model in our case [28].

The ECM structure is displayed in in Figure 2.6. In the ECM, each cell consists of essential components: the main capacitor C , the equivalent series resistance R_s , an additional resistance R_{s2} , a differential capacitance C_{diff} , and an inductance L . The resistance R_{s2} and C_{diff} are arranged in parallel to allow the model to effectively represent leakage currents that occur in a supercapacitor.

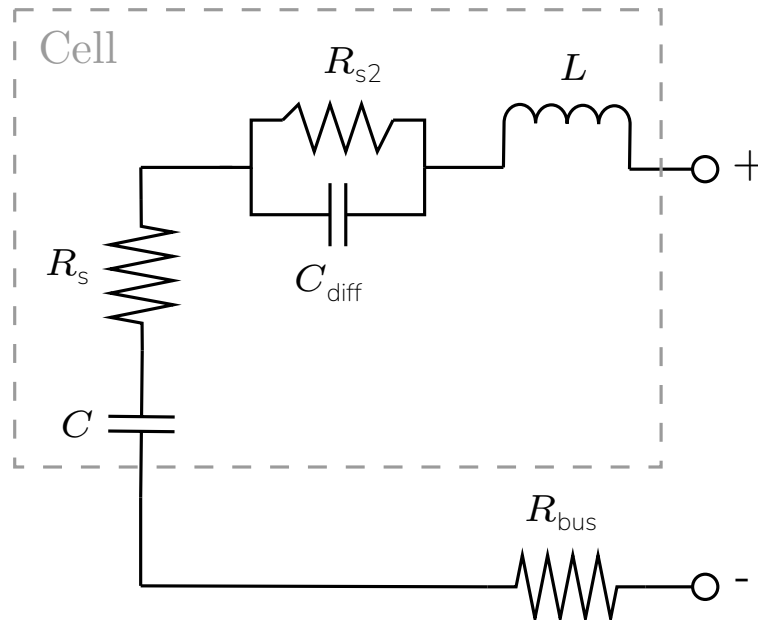


Figure 2.6: ECM of a supercapacitor

The model is designed to allow for an arbitrary number of cells to be connected in series. Users can specify the number of cells, as well as all other configurable parameters, through the mask, as shown in Figure 2.7.

The total capacitance of the stack is calculated by

$$C_{total} = \frac{C}{N_{cells}}, \quad C_{diff,total} = \frac{C_{diff}}{N_{cells}}. \quad (2.4)$$

The total equivalent series resistance increases with the number of cells in series according to

$$R_{s,total} = R_s N_{cells}, \quad R_{s2,total} = R_{s2} N_{cells}. \quad (2.5)$$

The stored energy of the stack in can be calculated by

$$E_{stored} = \frac{0.5 C_{total} V_{total}^2}{3600 \text{ s/h}}, \quad (2.6)$$

where V_{total} is the total voltage of the stack which is accessed in Simulink through a Voltage Measurement block.

To simulate the dynamic operation of a 1.5 MW supercapacitor, the values specified in Table 2.2 were used as input parameters for the mask and the remaining required values in the ECM in Figure 2.6.

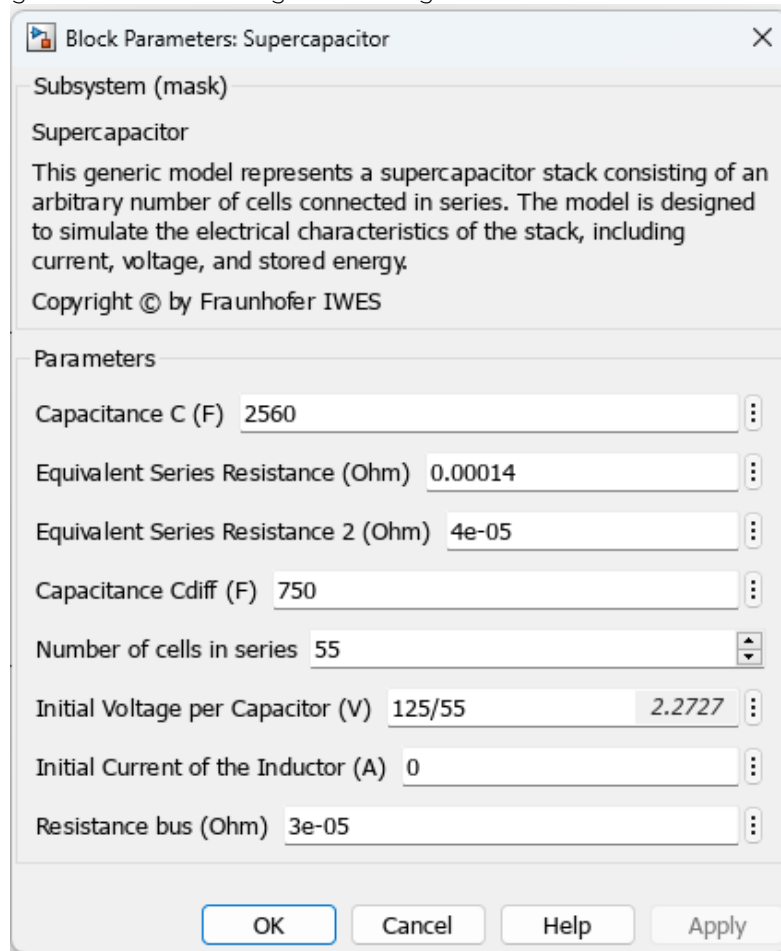


Figure 2.7: Mask with design parameters for the supercapacitor

The dynamic operation of the 1.5 MW supercapacitor when a current is applied is shown in Figure 2.8.

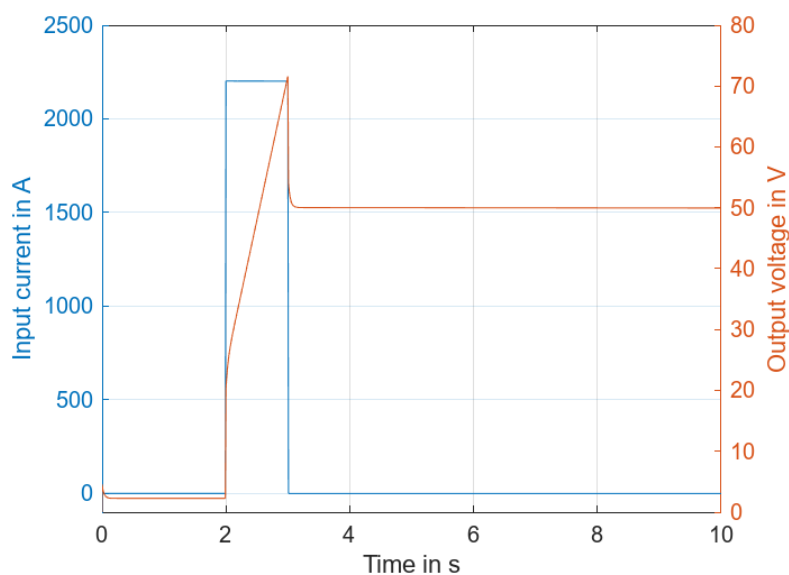


Figure 2.8: Dynamic operation of the 1.5 MW supercapacitor

Table 2.2: Parameters of a 1.5 MW supercapacitor.

Parameter	Symbol	Value
Capacitance	C	2560 F
Equivalent Series Resistance	R_s	140 $\mu\Omega$
Equivalent Series Resistance 2	R_{s2}	40 $\mu\Omega$
Differential Capacitance	C_{diff}	750 F
Number of cells in series	N_{cells}	55
Initial Voltage per Capacitor	V_i	2.27 V
Initial Current of the Inductor	A	0 A
Resistance bus	R_{bus}	30 $\mu\Omega$
Inductance	L	100 nH

2.3 Lithium-Ion Battery

Lithium-ion battery (LIB) modeling approaches often use ECM models, which can be classified into several types. A simple model with a constant voltage source and resistance fails to capture non-linear behaviors related to the state of charge (SOC). The Thevenin model, using resistors and capacitors, effectively represents transient and steady-state behaviors, with the second-order Thevenin model (2RC) capturing charge transfer, diffusion, and solid electrolyte interface. The 2RC is easy to interpret, can be modeled into simple mathematical equations, and allows for values to be obtained through simple experiments [14].

In this case, the 2RC was chosen to model a generic LIB. The ECM is displayed in Figure 2.9.

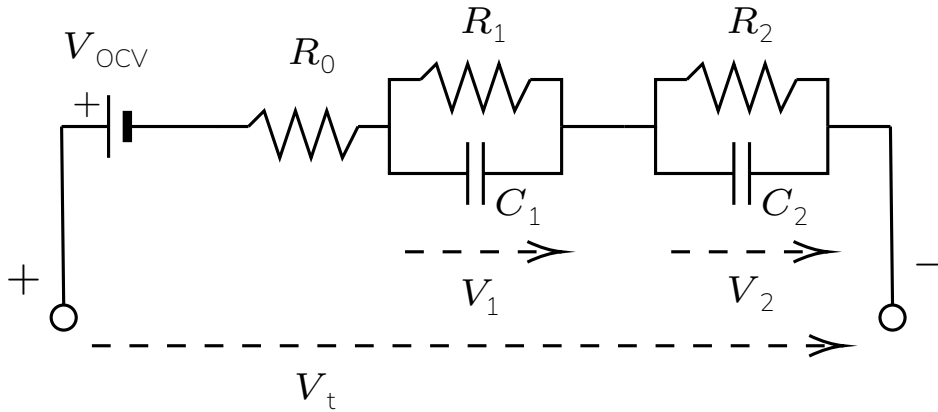


Figure 2.9: ECM of a LIB (own representation based on [26])

The model circuit consists of a voltage source, a series resistance and two RC parallel networks. This configuration captures the initial non-linearity caused by electrochemical polarization, characterized by equivalent capacity C_2 and electric resistance R_2 . Additionally, it accounts for the slower non-linearity due to diffusion, characterized by C_1 , R_1 . The voltage source represents the open circuit voltage V_{OCV} of the battery, the series resistance R_0 represents the internal resistance, and V_t indicates battery terminal voltage [2].

As described in [2], the 2RC can be expressed by

$$V_{t,j} = V_{OCV} - R_0 I_j - V_{1,j} - V_{2,j}, \quad (2.7)$$

with

$$V_{1,j+1} = \exp\left(-\frac{\Delta t}{R_1 C_1}\right) V_{1,j} + R_1 \left(1 - \exp\left(-\frac{\Delta t}{R_1 C_1}\right)\right) I_j, \quad (2.8)$$

and

$$V_{2,j+1} = \exp\left(-\frac{\Delta t}{R_2 C_2}\right) V_{2,j} + R_2 \left(1 - \exp\left(-\frac{\Delta t}{R_2 C_2}\right)\right) I_j, \quad (2.9)$$

where Δt is the sampling time and I_j is the current in the cell at instant j .

As described in [26], the SOC at instant j can be calculated by

$$\text{SOC}_j = \text{SOC}_0 + \frac{1}{C_{\text{rated}}} \sum_{i=0}^j I_i \Delta t, \quad (2.10)$$

where SOC_0 is the initial SOC, I is the current, and C_{rated} is the rated capacity of the LIB.

For the Simulink model, empirical data from an experiment known as the Hybrid Pulse Power Characterisation (HPPC) test was used. The cell used for the study is a LFP26650P by K2 Energy Solutions Inc., with a nominal capacity of $C_{\text{rated,ref}} = 2.6 \text{ Ah}$, a nominal voltage of $V_{\text{nom,ref}} = 3.2 \text{ V}$, and a voltage range of 2.00 V to 3.65 V. The results, which represent R_0 , R_1 , R_2 , C_1 , C_2 , and V_{OCV} as functions of the SOC, were incorporated into the model in the form of lookup tables and are utilized during the simulation for the corresponding parameters in (2.7)-(2.9).

To simulate, the characterizing values of the LIB are then entered into the mask in Simulink by the user, as shown in Figure 2.10.

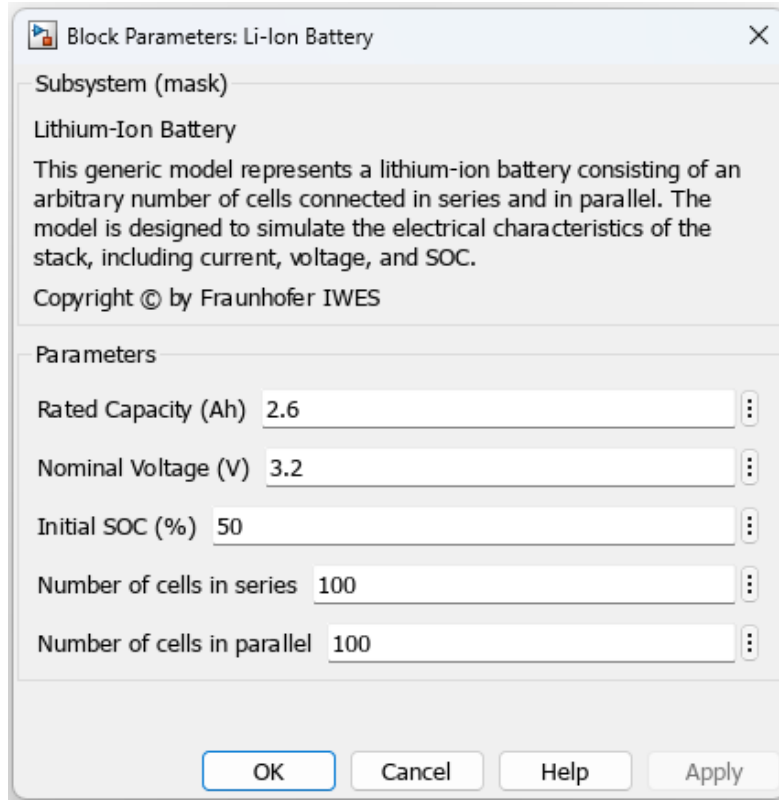


Figure 2.10: Mask with design parameters for the 1.5 MW LIB

For user inputs that deviate from the characterizing values of the measured cell ($C_{\text{rated,ref}}$ and $V_{\text{nom,ref}}$), the outputs of the lookup tables for C_1 , C_2 , and V_{OCV} are recalculated to obtain the new values C_{new} and $V_{\text{OCV,new}}$.

The outputs from the lookup tables for C_1 and C_2 are adjusted by

$$C_{\text{new}} = \frac{C_{\text{rated}}}{C_{\text{rated,ref}}} C_{\text{ref}}, \quad (2.11)$$

where C_{rated} is the user input and C_{ref} is the original lookup table output.

For the lookup table output of V_{OCV} , the adjustment is given by

$$V_{\text{OCV,new}} = \frac{C_{\text{nom}}}{C_{\text{nom,ref}}} C_{\text{OCV,ref}}, \quad (2.12)$$

where C_{nom} is the user input and $V_{\text{OCV,ref}}$ is the original lookup table output.

The user input of cells in series (n) and in parallel (m) is accounted for by

$$V_{\text{t,tot}} = V_t n, \quad (2.13)$$

and

$$I_{\text{tot}} = I m, \quad (2.14)$$

where $V_{\text{t,tot}}$ is the total voltage and I_{tot} is the total current of the stack.

The dynamic operation of a 1.5 MW LIB when a current is applied is shown in Figure 2.11. The input values shown in Figure 2.10 are used.

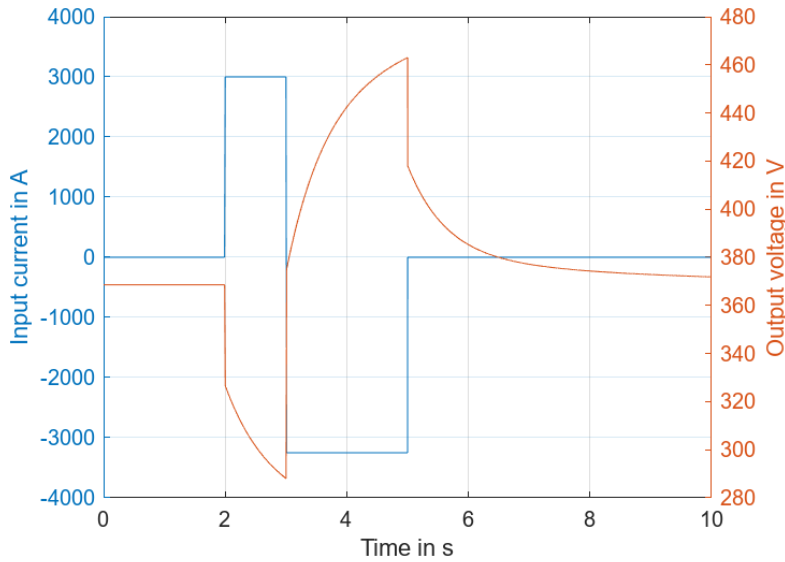


Figure 2.11: Dynamic operation of the 1.5 MW LIB

2.4 Hydro Pump

The modeling of the hydraulic pump considers its hydraulic behavior with its periphery and is based on the work of [13] and [1]. The hydraulic operating point is defined by the characteristic curves of the pump (2.16) and the system (2.17). Since the pump is directly connected to the pipe system the pressure heads of both elements must take the same value, thus:

$$H_{\text{per}} = H_{\text{pump}} \quad (2.15)$$

The characteristic curve of the pump links its pressure head H_{pump} (m), rotational speed of the pump ω (p.u.) and output flow Q (m^3/s):

$$H_{\text{pump}} = A\omega^2 - BQ^2 - C\omega Q - L\frac{dQ}{dt}, \quad (2.16)$$

with A , B and C the characteristic coefficients of the pump as given by the manufacturer or obtained experimentally and L the dynamic parameter for the fluid inertia.

Table 2.3: Parameters of a 160 kW hydro pump.

Parameter	Symbol	Value
Pump A coefficient	A	120 m
Pump B coefficient	B	$3865 \text{ s}^2/\text{m}^5$
Pump C coefficient	C	$0 \text{ s}/\text{m}^2$
Dynamic fluid inertia coefficient (pump)	L	100
Pump's inertia	J	$5 \text{ kg} \cdot \text{m}^2$
Transmission efficiency	η	0.9
Static head	H_0	100 m
Hydraulic losses coefficient	K	$60 \text{ s}^2/\text{m}^5$
Dynamic fluid inertia coefficient (periphery)	L_{per}	1000
Fluid density	ρ	$1000 \text{ kg}/\text{m}^3$
Acceleration of gravity	g	$9.81 \text{ m}/\text{s}^2$

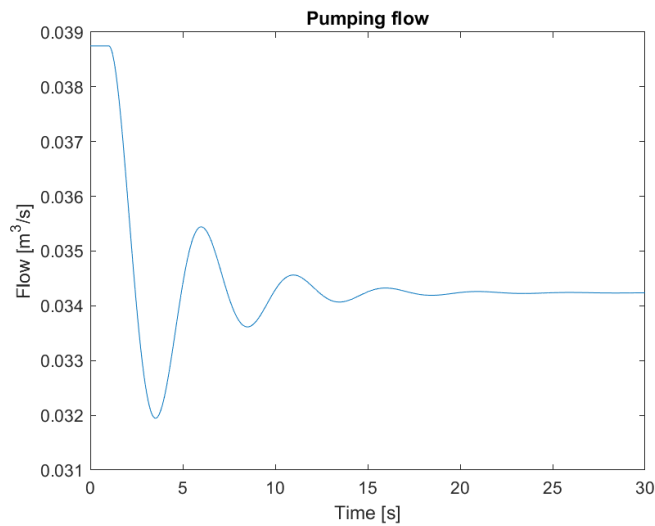


Figure 2.14: Dynamic operation of the hydro pump (Flow)

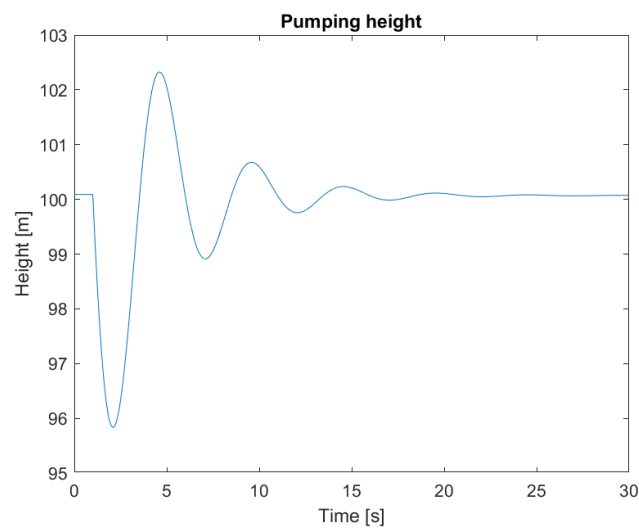


Figure 2.15: Dynamic operation of the hydro pump (Pressure)

The PV model is the standard Simulink component [11].

2.6 Capacitor

The standard capacitor model of Simulink is used [10].

2.7 Grid-Following Inverter

The grid-following control is a standard PLL control approach in dq-quantities [9].

2.8 Grid-Forming Inverter

The grid-forming control is based on a virtual synchronous machine (VSM). Fraunhofer IEE developed the model. The implementation is described [5]. The current limitation was extended and is achieved through temporary current control, which allows the grid-forming functionality to be maintained during a fault most of the time. The control structure is shown in Figure 2.16. Further information is given in [24]. In the provided model, no sequence separation is applied. The inertia provision is shown in Figure 2.17.

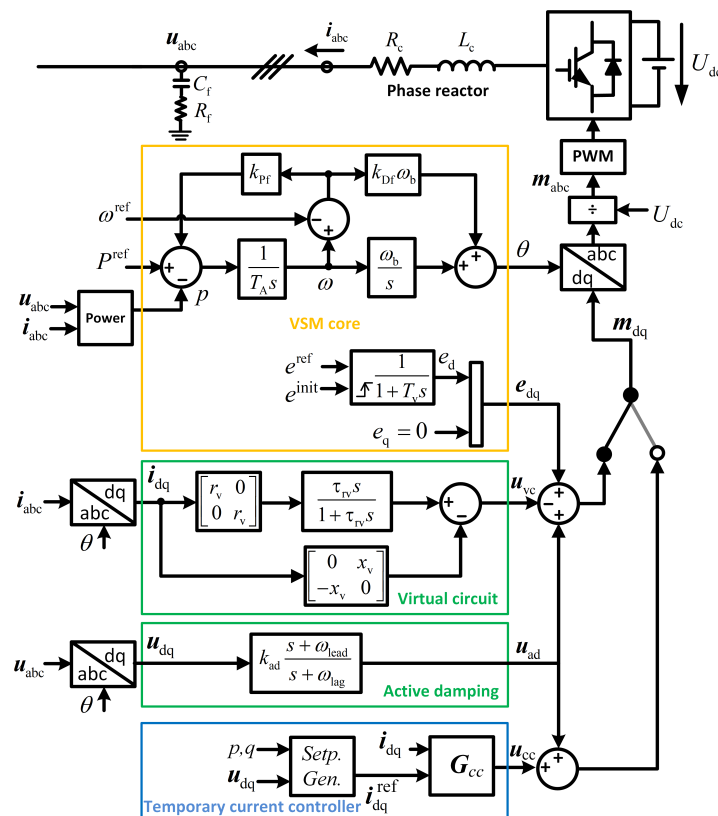


Figure 2.16: GFM control structure

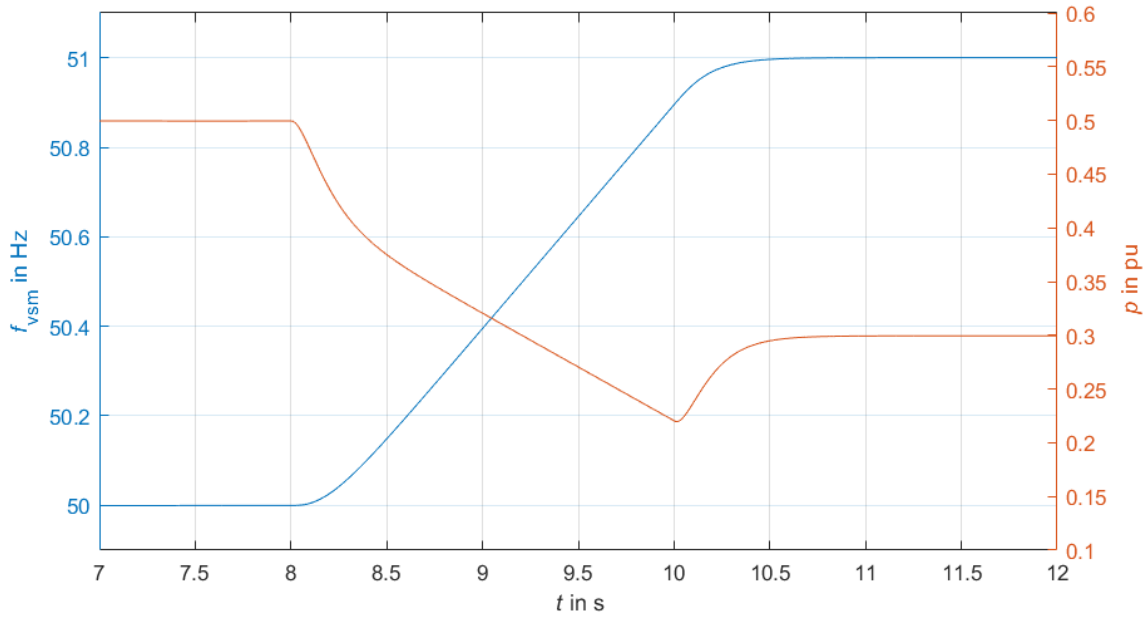


Figure 2.17: RoCoF event with 0.5 Hz/s and inertia response

2.9 Grid-Forming Inverter for Tailored Inertia

The theoretical background of and design considerations for ‘inertia tailored to the unit and the system needs’, short ‘tailored inertia’, can be found in [18]. Brief: ‘The contribution of inertia, conventionally expressed by the acceleration time constant T_A , becomes tailored to optimally exploiting resources while respecting their P limitations and keeping the maximum of network participants operational during extreme events.’

The technical description on how to modify a generic converter using a VSM control scheme to contribute tailored inertia in an interconnected system is given in [19]. The core converter model used here is the same as in Section 2.8, based on [5].

The model uploaded in https://github.com/AGISTIN-Project/AGISTIN_Project/tree/AsymInertia_UniKs_WS not only contains a converter but a whole grid subsection with three converters for tailored inertia, see Fig. 2.18. Thorough investigations have been conducted with the grid model. Results are shown and described in [18, 19]. After having established the mechanisms of tailoring inertia in the simulation model, the next step is to employ the modified converter model in the laboratory.

The subsections appended to this chapter describe details of the modelling which are not included in [19].

2.9.1 General Augmentation of the Grid Model: Frequency Measurement

(This section is a copy from the appendix of a draft of a monograph with the working title ‘Complementary Grid Forming as a Step Towards an Optimized Use of Resources in Frequency Stability’ authored by Walter Schitteck, University of Kassel, intended to be published in 2027.)

Besides the internal frequencies of the VSM which need not be measured, it is necessary to measure the frequency and voltage angle at buses of the network, e.g. of a load. Usually, a PLL (phase-locked loop) is employed to measure those quantities. In order to measure both quantities with the ability to follow rapid changes in the respective quantity as correctly as possible, two PLLs have been implemented: One PLL for f measurement (the upper PLL in Fig. 2.19), parameterized with a very short time constant. And

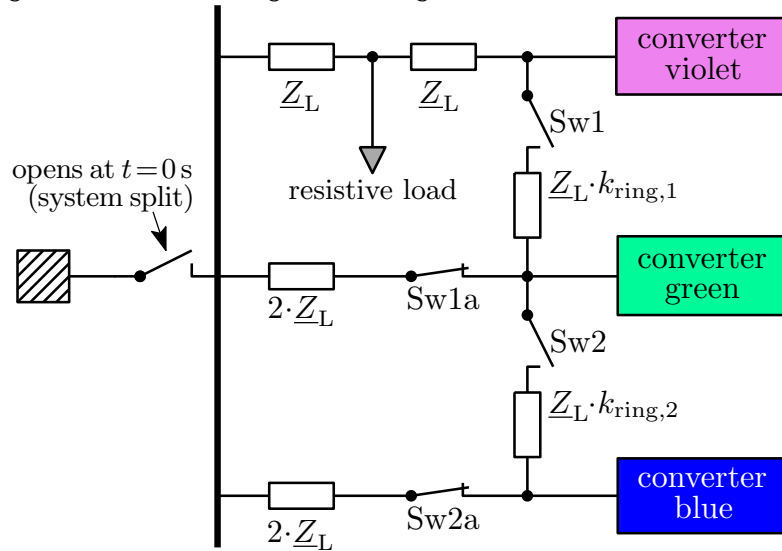


Figure 2.18: Grid section for investigation of tailored inertia

another PLL for tracking the (basically ever-increasing) phase angle theta (the lower of the two PLLs in Fig. 2.19), parameterized with an input voltage way below the actual voltage in the grid. Below the two PLLs in Fig. 2.19, a block for f measurement oriented at zero crossings of the voltage is implemented which outputs a new f value every 20 ms. The following description only looks at the f measurement by PLL.

The investigations include events where high positive or negative RoCoF values are caused by huge load steps accompanied by voltage-angle steps. In a realistic grid model, a PLL reacts on a voltage-angle step by letting its frequency output quickly jump between extreme positive and negative deviations from its former measurements. These spurious f values – as they will subsequently be called – carry no analysable information and lead to result plots with peculiar unclear f values. The objectives of the signal processing described subsequently are to reproduce the information in the measured f signal as correctly as possible and to keep the effects of spurious f values as short and as slight as possible.

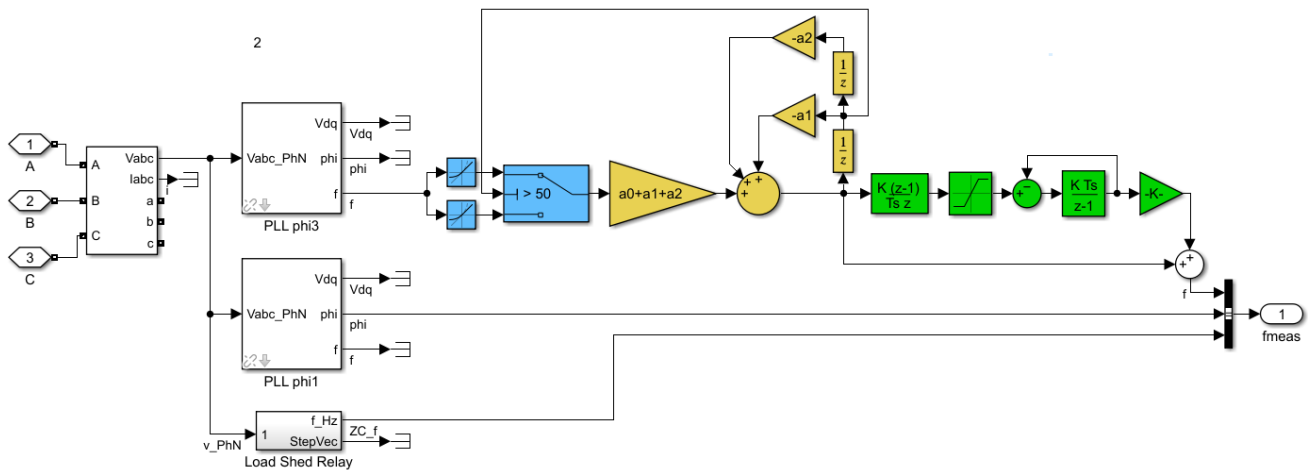


Figure 2.19: Frequency measurement including filtering.

The ramp-rate limiting (the blue blocks) at the output of the upper PLL is parameterized differently for departures from and rapprochement to f_{rated} . Departures are limited to ± 10 Hz/s whereas rapprochements are quasi unlimited to ± 1000 Hz/s. The effect of the asymmetric limits is that spurious f departures are not delayed in their return to the correct values. The parameterization is a compromise between suppressing spurious f reactions on voltage-angle steps and the ability of tracing extreme f departures

caused, e.g., by the P -confining current control (Section 2.9.2). If the latter is active for around 100 ms, f ramps in a range of not beyond ± 10 Hz/s are entailed. Much shorter activation times of, e.g., 20 ms entail even steeper f ramps, but the resulting (relatively small) f changes get swamped by spurious f values. Hence the ramp-rate limit ± 10 Hz/s for departures from f_{rated} .

Of course, the measured f signal still needs filtering. Averaging or a low-pass-filter generally have the disadvantage that (non-spurious) steep f changes are reproduced with more or less lagging f values. Therefore, a type of filter is chosen that retains the possibility of compensating f lags.

In continuous-time systems, a Bessel filter has a constant group delay, meaning that all relevant frequencies still represented in the filtered signal have undergone the same constant delay [29]. However, after applying the bilinear transform (Tustin's method) to a Bessel filter, its discrete-time correspondent has no constant group delay [20]. But there is a solution: An infinite-impulse-response (IIR) filter can be designed to behave for discrete-time signals like a Bessel filter does for continuous-time signals, i.e. produce an output signal with a parameterizable constant group delay. The IIR filter (the yellow blocks) has $\tau = 85$ leading to a group delay of $\tau \cdot 125 \mu\text{s} = 10.625$ ms and has the parameters

- $a_0 = 1$,
- $a_1 = -2 \cdot 2 \cdot \tau / (2 \cdot \tau + 3) = -1.9653179$,
- $a_2 = 2 \cdot \tau \cdot (2 \cdot \tau + 1) / ((2 \cdot \tau + 3) \cdot (2 \cdot \tau + 3 + 1)) = 0.9657166$.

The constant group delay is the precondition for compensating the f lag in the filter output in case of steep f changes. The compensation signal added at the f output of the subsystem is assembled by the green blocks: The discrete-derivative block outputs the RoCoF in Hz/s of the filtered f signal. The saturation block behind it limits the compensation to RoCoFs in the range of ± 4 Hz/s in order to not amplify spurious f movements or f glitches. The low-pass filter with the integrator takes the average of very quick changes in the RoCoF with a time constant of 1 ms. The green gain block multiplies the average RoCoF value in Hz/s by the group delay to get the adequate compensation value.

For imagination: In case of a constant RoCoF, the group delay of the IIR filter (yellow blocks) effects that the filter output shows the f value that has been correct 10.625 ms before. In case of a known signed RoCoF, the signed f progress during the delay is calculated and added to the filter output to get a final f value that is as correct as possible, particularly if rapid f movements are rather the rule than the exception.

2.9.2 General Augmentations of the Generic Converter Model

(This section including all subsections is a copy from the appendix of a draft of a monograph with the working title 'Complementary Grid Forming as a Step Towards an Optimized Use of Resources in Frequency Stability' authored by Walter Schitteck, University of Kassel, intended to be published in 2027.)

Fast Voltage Regulator

The disruption of huge P flows, which are one of the focuses of investigations with the converter, locally leads to severe voltage deviations which must be returned into the regular voltage range within tens of milliseconds. The only equipment able to regulate the voltage are the converters under investigation.

Regularly, synchronous machines and power-electronic converters employ some kind of continuously-working voltage control. Aside from very simple grid structures, these controls need an analysis of oscillation modes and individually parameterized damping. For the conducted investigations, a huge variety of voltage levels, cable/line types, and line lengths was envisaged, which demanded for a voltage control without the need of reparameterization between simulations. This has been achieved with the fast voltage regulator in Fig. 2.20. However, this is a solution specifically designed for the investigations with this model and needs explanation.

The design of the voltage regulator is non-linear and discontinuous, most likely to be associated with a bang-bang control. Principle: The output V_{Rout} of the subsystem is fed from the green integrator and is added (outside the subsystem) to the default level of the internal voltage of the VSM. The output of the

- The right-hand input of the blue multiplier boosts the multiplication by a factor of 12.5 for a maximum of 1 ms (i.e. 8 times the sample time) in the moment when U_{abs} leaves the range 0.9 p.u. to 1.08 p.u. In most of these cases, the middle input has the value 10 which yields a multiplication by 125.

There are circumstances under which the input of the green integrator is blocked and therefore its output frozen:

- While the P -confining current control (see Section 2.9.2) is active, the upper input of the green multiplier is set to 0 instead of 1.
- The yellow adder and integrator form a low-pass filter that tracks the sign and amplitude of the pulses at the middle input of the green multiplier. The five blocks above the yellow adder effect that the signed amplitude of a pulse is registered with an integrator time constant of only 1 ms but decays with a time constant of 10 ms after the end of the pulse. The three blocks between the yellow integrator and the green multiplier effect that arbitrary pulses of the opposite sign pass through to the green integrator but pulses of the same sign must have an amplitude the higher the quicker they follow the preceding pulse to pass through to the green integrator. The intended effect is to employ very large pulses for fast response times of the voltage control on a large voltage deviation but – as far as possible – avoid overshoots of the voltage. (The remaining blocks connected to the green adder simply avoid a division by zero.)

Everything said in this item holds for negative as well as positive voltage deviations.

The voltage regulator subsystem can be removed from the VSM with no effect except that everything described here no longer works. Of course, its former output connection must be replaced by a constant value of 0.

Fast P -Confining Current Control

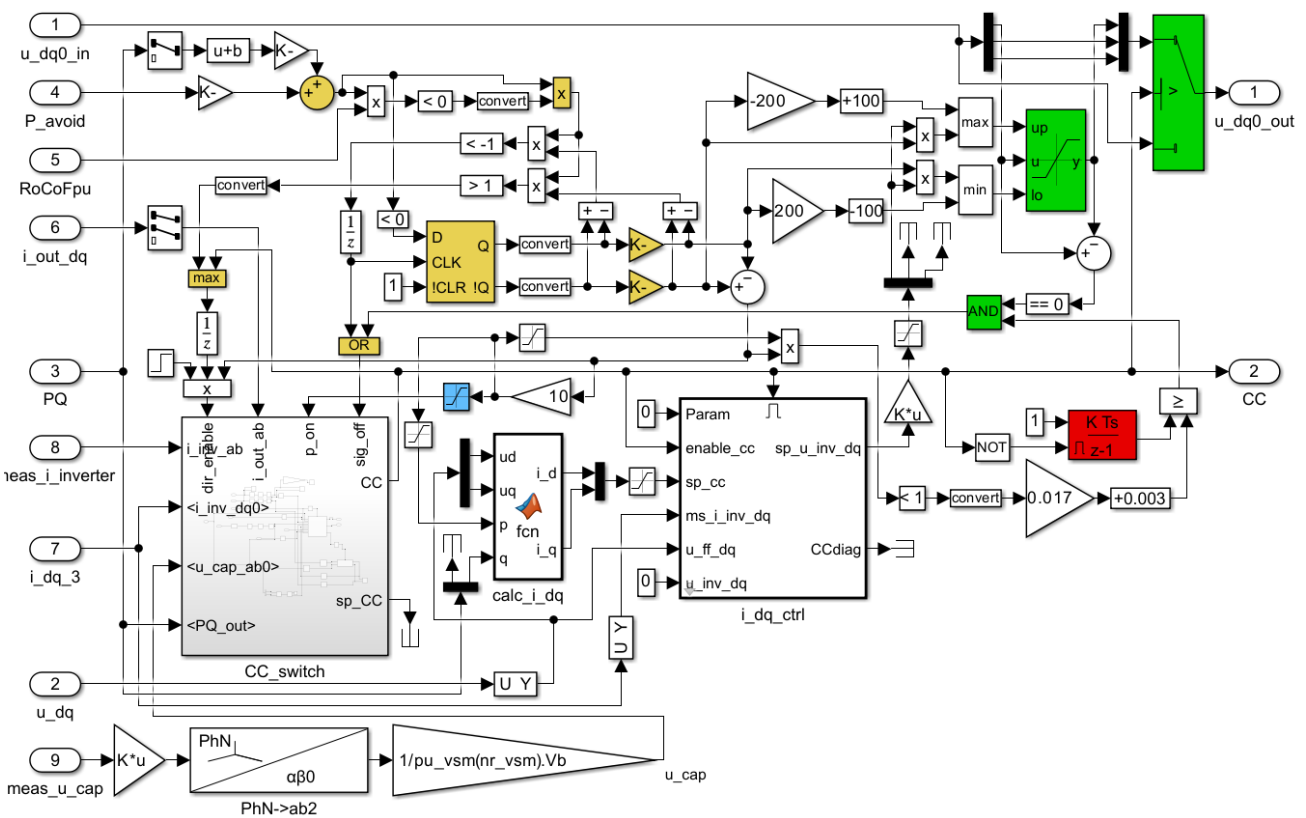


Figure 2.21: Subsystem CurrentControl.

Fig. 2.21 shows the subsystem ‘ P -confining I control’. It contains the two Simulink subsystems `CC_switch` and `i_dq_ctrl` and between them the Matlab function `calc_i_dq`. Subsequently, boldly printed terms in-



indicate the only or first and/or main explanation given to an element in Fig. 2.21. The exact term can be searched throughout the subsection to find additional parts of the text where explanations concern that same element. The four paragraphs of the following descriptions go counter-clockwise through the four quarters of Fig. 2.21.

Roughly the top left quarter of Fig. 2.21 contains the signals and logic for the decisions about deactivation, preparation for activation in direction of rising or falling P , and start of the current control. Moreover, the parameterization for the triggering and the operation of the current control are calculated here.

- The preparation for activation (or, in rare cases, a premature termination and preparation for activation in the opposite confinement direction) of the current control takes place whenever the signed output of the yellow multiplier takes an absolute value >1 . This is only possible when the input RoCoFpu has the opposite sign to the output of the yellow adder AND the signed output of the yellow adder has an absolute value >1 .
- P_{thres} (not in Fig. 2.21) is the signed value by which the P limitation of the converter has to be exceeded to actually trigger the current control. The actual parameterization for investigations with the model has been $P_{\text{thres}} = \pm 0.04$ p.u. Whereas this quantity plays a role in the next items, the process of the triggering itself is explained further below with the bottom left quarter of Fig. 2.21.
- Always only one of the two inputs of the yellow adder can become unequal zero:
 - If the total P variation range of the converter is greater or equal 0.4 p.u., only the upper path – processing the input PQ – is relevant. The signed output of the yellow adder takes an absolute value >1 if the measured P of the converter is closer to one of the margins of its total P variation range than to the middle of that range.
 - If, however, the total P variation range of the converter is below 0.4 p.u., only the lower path – processing the input P_avoid – to the yellow adder is relevant. Its signed output takes an absolute value >1 if $|P_{\text{avoid}}| > |P_{\text{thres}}|$.

As mentioned above, the output of the yellow multiplier can only take a value unequal zero if the input RoCoFpu has the opposite sign to the output of the yellow adder. This requirement inhibits the triggering of the current control in cases where the instantaneous voltage-angle change is not the cause of an exceedance of the trigger threshold.

- The output Q of the yellow D-flipflop indicates the direction of activation of the current control – before and after it is triggered. $Q=1$ is for a rising f and directs the P confinement to the lower end of the P variation range (in generator view), i.e. highest P consumption or lowest P feed-in, depending on the kind of device. Correspondingly, $Q=0$ is for a falling f and directs the P confinement to the upper end of the P variation range, i.e. highest P feed-in or lowest P consumption.
- The outcome of a value >1 or <-1 of the output of the yellow multiplier depends on the state in which the yellow D-flipflop is found:
 - If the state of the the yellow D-flipflop does not match the desired state expressed by the sign of the output of the yellow multiplier, the $\frac{1}{2}$ block (i.e. delay of one time step) on the way to the clock input of the yellow D-flipflop will give a positive slope to the clock at the next time step, and the flipflow will take the new state at the next time step which makes the next item true then. If in that situation the current control is active – and directed oppositely – at the moment, its operation will come to a premature end via the yellow OR block.
 - If the yellow D-flipflop has the desired state expressed by the sign of the output of the yellow multiplier AND the P confining current control is parameterized (the two yellow gain blocks) for protecting the corresponding end of the P variation range, then the path through the left input of the yellow max block enables the triggering of the current control in the corresponding direction, see next paragraph.

Roughly the bottom left quarter of Fig. 2.21 is dedicated to the triggering and termination of the current control and to continuously providing the signals needed.

- The input dir_enable of the subsystem CC_switch deactivates the current control when its value is zero. A value +1 enables triggering and operation around the most positive (in generator view) P whereas a value -1 does the same around the most negative P of the variation range.
- In the state when triggering is enabled (previous item) but has not yet happened, the input p_on of



the subsystem CC_switch is to be provided with the P trigger threshold for activation of the current control. The value with the correct sign, marginal P value $+ P_{\text{thres}}$ comes via the blue saturation block which is parameterized with both possible values as the upper and the lower limit.

- After the current control has been triggered, the output CC of the subsystem CC_switch changes its value from FALSE (0) to TRUE (1).
- One crucial signal for the activated current control is its P setpoint value. It is calculated in the same way as with the blue saturation block and fed into the input p of the Matlab function block calc_i_dq. The working principle of the P -confining current control demands that that P value be between the P trigger threshold and the pertinent limit of the P variation range. The actual parameterization for investigations with the model has been 0.005 p.u. beyond the P limit value. The corresponding Q setpoint value is fed from the measured Q . Thereby, no intentional modification is envisaged but a drift of the value is possible and mostly actually happens.
- From its four input values, the Matlab function block calc_i_dq calculates the instantaneous values i_d and i_q of the I setpoint of the current control. Roughly the bottom right quarter of Fig. 2.21 contains the controls for operation and regular termination of the current control.

- When the current control is active, the subsystem i_dq_crtl is activated by the value TRUE (1) at its activation input (top) and the input enable_cc. The other inputs sp_cc (i_d, i_q setpoint), ms_i_inv_dq (measured i_d, i_q), and u_ff_dq (measured u_d, u_q) provide the signals for continually calculating the output value sp_u_inv_dq (controlled u_d, u_q value for the PWM of the converter) of subsystem i_dq_crtl. In [25], the current control implemented in the subsystem i_dq_crtl has been introduced. In [24, p. 3], a flowchart of the current-limiting strategy is shown.
- The red integrator is used for masking a spurious termination signal after very short time. For that purpose, two different time intervals are used: If the pertinent limit of the P variation range is less than 0.1 p.u. away from the P setpoint of the converter, the masking time is 20 ms, otherwise it is only 3 ms. Roughly the top right quarter of Fig. 2.21 contains the modification of the input signal u_dq0_in in the active state of the current control. The activated current control only takes influence on u_d .
- While the current control is activated, the upper input of the green switch block is active. In all other situations, the lower input is active and the upper input may take arbitrary values without having an effect.
- The upper and lower limit of the green saturation block are managed by the outputs of the two yellow gain blocks and are relevant only in the active state of the current control:
 - When the upper of the yellow gain blocks has an output of 1 (meaning rising f and pertaining to the lower end of the P variation range), the lower limit of the green saturation block takes the u_d value offered by the current control. The upper limit of the green saturation block retains its default value, +100.
 - When the lower of the yellow gain blocks has an output of 1 (meaning falling f and pertaining to the upper end of the P variation range), the upper limit of the green saturation block takes the u_d value offered by the current control. The lower limit of the green saturation block retains its default value, -100.
- The fact that the current control only provides a u_d limit and not a value u_d must take, allows for a simple exit from the current control: As soon as the other components of the modified VSM control have managed to bring u_d to a value inside the limit set by the current control, input and output of the green saturation block take identical values. Via the green AND block and the yellow OR block, this information terminates the current control.

Very few signal paths relevant for the P -confining current control are not included in the subsystem. Subsequently, these are explained, without referring to additional figures.

The output CC of the subsystem 'P-confining I control' directly goes into input sig_on of the subsystem VSM_Ebene_3. In that subsystem, it influences two crucial function blocks.

- As long as sig_on is TRUE (meaning that the current control is active), the output signal of the Fast Voltage Regulator – see Section 2.9.2 – is frozen. When sig_on becomes FALSE again, the voltage

regulator continues to work, starting from the frozen value.

Background: As long as u_d is determined by the current control, the voltage regulator would not be able to enforce differing values for $u_{d,q}$. In this way, voltage control can continue smoothly after termination of current control.

- As long as sig_on is TRUE, $T_{P,base}$ is switched from its parameterized value to a value of 2 s. This helps the VSM frequency and voltage angle undergo the changes necessary for terminating the current control as quickly as stably possible.

The current control subsystem can be removed from the VSM with no effect except that everything described here no longer works. Of course, its former input u_{dq0_in} must be connected to the former connection of its output u_{dq0_out} and the former connection of its output CC must be replaced by a constant value of FALSE or 0.

Additional Inertia in Case of Active LFSM

Preliminary note: This subsystem must not be omitted without replacement; otherwise, inertia can no longer be parameterized by regular T_P values but only by internal T_P values.

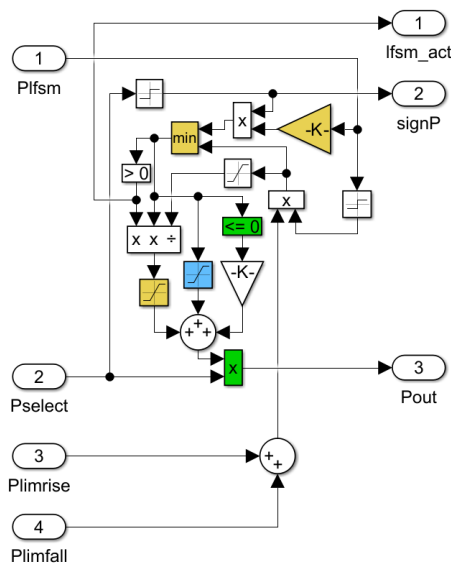


Figure 2.22: Subsystem for additional inertia in case of active LFSM-O/U.

This subsystem, Fig. 2.22, is in its default state as long as

- neither LFSM-O nor LFSM-U is active OR
- LFSM-O or LFSM-U is active and f is constant or still departing from f_{rated} .

That default state is characterized by a value ≤ 0 at the input of the green comparator block. The gain block below it has a gain of 0 in case of internal T_P values, otherwise (regular T_P values) a gain of 1. In the latter case, the inertia-power values at input Pselect are handed over to the output Pout without modification – as long as the default state of this subsystem persists.

The functioning of the remainder of this subsystem is oriented at the requirements given in [22, p. 26]. The default state of this subsystem can only be left if both (!) inputs of the yellow min block take values > 0 .

- The lower input of the yellow min block can only become positive if the input Plfsm takes the same sign as the addition of the inputs Plimrise and Plimfall. Considering the sign of the attained f deviation from f_{rated} , that condition is only fulfilled if the limit for the inertia power of the converter is more restrictive (or even zero) for a rapprochement of f to f_{rated} than for an f movement enlarging the f deviation.
- The upper input of the yellow min block can only become positive if the sign of input Pselect is opposite to the sign of input Plfsm, meaning that a rapprochement of f to f_{rated} is under way. If, however, additional inertia (being the purpose of this subsystem) is parameterized to remain inactive, the yellow

gain keeps the upper input of the yellow min block 0, and the subsystem can never leave its default state.

A positive value at the output of the yellow min block means:

- The path via the green comparator block becomes inactive.
- In case of internal T_p values, the blue saturation block lets arbitrary positive values pass. Consequently, output P_{out} takes inertia power multiplied from the input P_{select} and the addition of the inputs $P_{limrise}$ and $P_{limfall}$. Outside this subsystem, the value of P_{out} adds to the unmodified inertia power resulting from the pertinent limit $P_{limrise}$ or $P_{limfall}$, as required in [22, p. 26].
- However, in case of regular T_p values, the yellow saturation block lets values between 0 and 1 pass. The values at its input are lower than 1 only in case that the LFSM power is insufficient, i.e. the f deviation from f_{rated} is relatively small. This is only a rough measure; the pertinent P limit restricting the sum of LFSM and (oppositely signed) inertia will enforce that P limitations are respected (outside this subsystem).

Everything described above together with the requirement in [22, p. 26] puts the correct performance of this subsystem under the precondition that the signed input P_{select} be provided with symmetrical absolute P values for both RoCoF signs – which may, however, be arbitrarily tailored and may result from regular or internal T_p values. The consequence of this precondition is that the provision of additional inertia is straightforward only for converters contributing unidirectional inertia with appropriate P limits. In other cases of asymmetrical inertia, only internal T_p values can be used but not regular ones. Fortunately, everything that can be done with regular T_p values can also be done with internal T_p values.

Two outputs of the subsystem have not yet been mentioned:

- The output $lfsm_act$ takes the value TRUE as long as additional inertia is actually deployed.
- The output $signP$ always takes the sign of input P_{select} .

Both outputs can be employed for different ways of activating the subsystem described in Section 2.9.2.

Reduced Inertia For Fast Return From Extreme Frequencies

In unfavourable conditions, particularly if LFSM-U/O contributions in the grid have mentionable time constants and the P limit of the considered device is active while f is farthest from f_{rated} , an extreme f excursion may tend to remain outside the f range for regular operation of the device for several seconds. However, the expectation in such a situation is that every device contributing inertia and LFSM arrange its return towards f values closer to f_{rated} as rapid as possible to preserve the chance of an f recovery before more and more devices regularly disconnect themselves due to the f excursion, cf. [22, p. 26]. In thus unfavourable conditions, the regular T_A respectively T_p values ([18]) stand against (i.e. are too large for) a sufficiently rapid decline of the f deviation. That's the point where the subsystem for reduced inertia for fast return from extreme frequencies comes into play, Fig. 2.23.

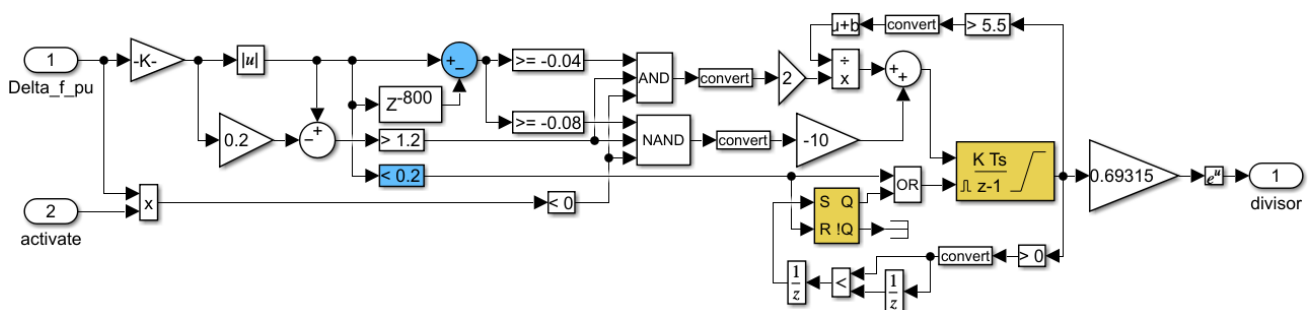


Figure 2.23: Subsystem for reduced inertia for fast return from extreme frequencies.

By default, the output of the subsystem has the value 1. Outside the subsystem, it is connected to the divisor input of a multiplier/divider block whose other input gets the unmodified P signal of the inertia contribution of the device. The lower input of the subsystem must directly be connected to the output $signP$ of the subsystem ‘Additional Inertia in Case of Active LFSM’ (Section 2.9.2) which carries the sign



of the inertia signal, corresponding to the sign of the f movement. Only when the sign of the inertia signal is opposite to the sign of the f deviation from f_{rated} (i.e. f is on the way of returning from an f excursion), the subsystem becomes active, no matter how slight the RoCoF. Hence, if RoCoF values are mentioned subsequently, they always pertain to the f movement back towards f_{rated} . The subsystem works by interpreting the Δf values at its upper input, the f deviation from f_{rated} . The leftmost gain block transforms the unit of Δf from p.u. to Hz. The blue comparator activates the reset of the yellow integrator whenever $|\Delta f| < 0.2$ Hz, and the output of the subsystem then takes its default value 1. The yellow integrator has a gain of 1 and the values 0 and 10 as its limits.

The blue adder continuously compares the absolute f deviation with the value it had 100 ms before. Hence, its output indicates 1/10 of the averaged RoCoF during the last 100 ms as always negative values (as long as the subsystem is active). The output of the yellow integrator can only increase if the central AND block has a TRUE output, which is the case if f is outside the range 49.0 Hz to 51.4 Hz and the absolute value of the RoCoF is within the range ± 0.4 Hz/s. In that case, the subsystem is required to make the f movement steeper, and the yellow integrator continuously increases its output by a rate of 1 every 0.5 s. That means the output of the subsystem doubles its value every 0.5 s.¹ As soon as the integrator output reaches a value of 5.5 or larger, the rate by which it increases is halved, i.e. the output of the subsystem doubles its value every second. The NAND block below the AND block has a FALSE output value during this phase since all its inputs are TRUE.

The effect of continuously bringing the inertia-related P down to smaller fractions of its intended value is that the initially slight absolute RoCoF values of the f movement back towards f_{rated} get larger and larger. As soon as the RoCoF leaves the range ± 0.4 Hz/s, the AND block makes its output FALSE, and the yellow integrator keeps its output value unchanged. Due to the changing internal LFSM signal and to external influences, the RoCoF will hardly remain constant but drift to lower or higher values. In case the RoCoF leaves the range ± 0.8 Hz/s, the NAND block will make its output TRUE, and the yellow integrator will decrease its output with a rate of 1 every 100 ms, but only until the RoCoF comes back into the mentioned range. If, however, the RoCoF comes back into the range ± 0.4 Hz/s, the AND block will make its output TRUE again, and the yellow integrator will increase its output again. In an exceptional case where f remains outside the range 49.0 Hz to 51.4 Hz, the sign of the inertia signal (input activate) will eventually change, and the lower input of the NAND block is no longer TRUE and it will bring the output of the yellow integrator down. Regularly, the manipulation of the inertia-related P ends when f returns to the range 49.0 Hz to 51.4 Hz. Then, the NAND block makes its output TRUE, and the yellow integrator decreases its output back to zero. As soon as this state is reached, the yellow integrator shall not start to increase its output again. This is achieved by the yellow SR flipflop which becomes active when the yellow integrator reaches the value 0 and is released only when f is back in the range 49.8 Hz to 50.2 Hz again.

The reduced-inertia subsystem can be removed from the VSM with no effect except that everything described here no longer works. Of course, the former connection of its output must be replaced by a constant value of 1.

Compensation of f Forerun Caused by Feedforward Damping

The converter design does not rely on $P(f)$ damping [12, p. 5] [27, pp. 581f] [15, p. 1224]. That makes the converter eligible for applications without access to storage, such as renewable generation or pure loads. Moreover, for operation in an interconnected system, the parameterizable $P(f)$ behaviour of the device offers all degrees of freedom for adaptation to grid-code requirements and entails no constraints resulting from damping requirements.

In the converter, angular feedforward damping is implemented [21, pp. 10f] [4, p. 5] [8, p. 7] [16, p. 928] [23, p. 60] [3, p. 121]. The damping is realized via modification of the voltage angle of $\underline{V}_{P\text{W}\text{M}}$, the voltage at the PWM point. Whenever f is changing, that kind of damping causes an f forerun proportional to the RoCoF. For a converter operated in an interconnected system such as the Central-European synchronous

¹The function 2^u as a Simulink block does not exist in Matlab version R2022a and has been replaced by calculating $e^{u \cdot \ln(2)}$.

area, the f forerun can be neglected as long as the interconnection remains intact. But in case of a system split, steep f changes can occur and the accompanying f forerun can take values of more than 0.2 Hz. As long as converters with angular feedforward damping are rather the exception than the rule, other grid-forming devices will not let the f forerun propagate throughout the grid, and converters using that damping will get a lagging inner f . But research about a new technology should always take into account that the object of investigation could (intermittently) dominate the grid in future years. And in that case, the f forerun could, e.g., lead to unnecessarily early activation of under-frequency load shedding. Hence, a compensation of the f forerun is necessary.

Of course, the design of the compensation must ensure that the damping characteristics are not impaired. The simple suppression of the f forerun is not an option because that would completely foil the intended damping. Similarly, investigations with frequency-dependent attenuation of the f forerun led to weakened damping. The guideline for keeping the damping unimpaired is that there must be no correlation between the compensation signal and the damping signal or the instantaneous RoCoF (to which the latter is proportional). Actually, the compensation subsystem derives its output signal only from conditioned information about the f development since the beginning of its excursion. The thus found solution for a damping compensation has ultimately been incorporated in the converter model, shows no evidence of weakening the damping and succeeds in excluding mentionable f foreruns at RoCoFs within the range ± 4 Hz/s when the resulting frequency deviation takes values beyond ± 0.8 Hz. The damping compensation described below has been used since November 2024 in all simulations with the converter, and in not a single one of all investigations, any suboptimal effects of it could be noticed. Becoming aware of such effects is easy because the damping compensation can be switched off by parameterization which has always been done when the cause of a peculiarity was unclear at first.

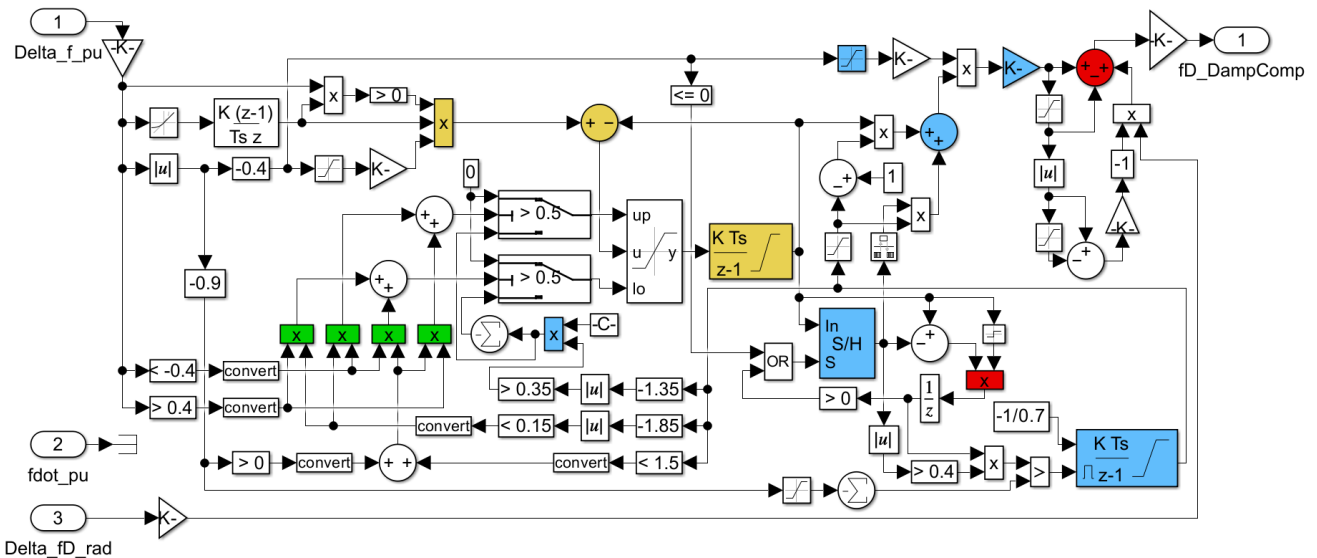


Figure 2.24: Subsystem for compensation of f forerun caused by feedforward damping.

Subsequently, **boldly printed** terms indicate the only or first and/or main explanation given to an element in Fig. 2.24. The exact term can be searched throughout the subsection to find additional parts of the text where explanations concern that same element.

In principle, the damping compensation, Fig. 2.24, calculates a compensation signal at output `fD_DampComp` out of its upper input `Delta_f_pu`. The pivotal element in the assembly of the compensation signal is the yellow integrator in the middle of Fig. 2.24 with a time constant of 10 ms. Its output is the result of the f changes that took place since the damping compensation left its default state. The default state of the input and the output of the yellow integrator is zero. Together with the yellow adder, the yellow integrator forms a low-pass filter.

Whenever the yellow integrator departs farther from zero, the blue sample&hold block gets a **TRUE** sample input to follow the output of the yellow integrator. Consequently, whenever the yellow integrator



only keeps its value or takes a turn towards zero, the blue sample&hold block holds its output value.

The blue integrator has an initial output value of 2.001 and remains in its reset state as long as the yellow integrator is still departing farther from zero or more or less keeping its value. In that state, the raw value from which the compensation signal is calculated comes from the output of the blue sample&hold block whose value is propagated to the output of the blue adder. The blue saturation block together with the subsequent gain block effects that the output of the blue adder is multiplied with a value 0...1 while the inner f of the converter is 400...800 mHz above or below f_{rated} . The blue gain block multiplies the assembled value by the proportionality factor of the f forerun so that the output of the blue gain block carries a signal in rad/s eligible for a 1:1 compensation. However, the red adder via the saturation block next to it diminishes that signal by the rad/s equivalent of ± 40 mHz which is deemed to be always tolerable as an f forerun. The gain block at the output fD_DampComp has a gain of 1 if the damping compensation is parameterized to be active, otherwise of 0. Outside this subsystem, the output fD_DampComp is subtracted from the damping signal to achieve the compensation.

The lower input Delta_fD_rad of the subsystem carries the not yet compensated damping signal. The Simulink blocks gathered below the red adder achieve a parameterizable damping amplification in all situations when no damping compensation is needed. The damping amplification is faded out linearly with a factor of 1...0 when the output of the blue gain block goes through the rad/s equivalent of $\pm 20... \pm 40$ mHz.

Up to here, the description has covered the departure of f from f_{rated} and the assembly of the compensation signal until its value has reached the appropriate magnitude. Subsequently, several qualitatively differing f developments can occur. The blue integrator is the pivotal element to initiate the necessary measures, and most of these will change the upper and/or lower limit of the dynamic saturation block in front of the yellow integrator. If one of the four green multipliers is mentioned, the counting is from left to right. With the default output 2.001 of the blue integrator, the four green multipliers initially keep their outputs 0, and only the blue multiplier gives the dynamic saturation block the symmetric limits mentioned above. The following cases need explanation:

- In case of rapid and partly reversal changes in the P flow of the converter during the f departure from f_{rated} , the yellow integrator may change its output value back and forth. The blue sample&hold block will not follow these changes but always keep the value which has been farthest from zero. That means the compensation signal does not follow the rapid changes but only departs further from zero whenever necessary.
- In the uncommon case that the f movement undergoes no mitigation or becomes steeper yet, the mechanisms already described keep the compensation adequate.
- As soon as f is more than 0.9 Hz above or below f_{rated} – which will occur relatively quickly in case of the previous item –, the third or fourth of the green multipliers (depending on the sign of the f deviation) ensure that the dynamic saturation block inhibits any further departure of the yellow integrator from zero. (Its rapprochement towards zero is still enabled.)
- In most cases, the f movement is mitigated, e.g. by $P(f)$ mechanisms inside and/or outside the converter. During the first phase of such mitigation, the departure of f from f_{rated} still continues but the output of the yellow integrator starts returning towards zero. The above description has made clear that the blue sample&hold block will not follow but keep the compensation value unchanged. This is reasonable not only with respect to stability but also because a temporary overcompensation is more acceptable than too weak of a compensation in unfavourable circumstances. (Furthermore, in the exceptional case that the f movement disrupts the mitigation and becomes steeper than any time before, the compensation value will adapt adequately.)

In that first mitigation phase, an additional mechanism is initiated, under one condition: The f movement must have had a certain minimum steepness, expressed via the minimum absolute value 0.4 (Hz/s) of the signed output of the blue sample&hold block. Then, the reset of the blue integrator is released according to one of two criteria which can be distinguished by the value of the lower input of the comparator in front of the reset input of the blue integrator:

- The simple criterion: If f is no more than 0.91 Hz above or below f_{rated} , the lower comparator input has the value -0.01 . Then, the output of the red multiplier need only take such slightly negative



value (meaning that the yellow integrator has made a significant move towards zero) to release the reset of the blue integrator.

- If, however, f is more than 0.91 Hz above or below f_{rated} , the less simple criterion becomes pertinent: The lower comparator input linearly goes through the values -0.01 to -0.3 when the absolute f deviation is 0.91 Hz to 1.2 Hz. Beyond that f deviation range, the comparator input remains at the value -0.3 . Hence, the yellow integrator must make an accordingly more significant move towards zero to release the reset of the blue integrator.

In case the reset of the blue integrator is actually released, it ramps down from its default value 2.001 with a gain of $-1/(0.7\text{ s})$. At any time during that rampdown, the reset of that integrator can be reactivated, namely when the yellow integrator comes back closer to the value of the blue sample&hold block. If, however, the rampdown continues to the lower limit 0 of the blue integrator within a total duration of 1.4 s, the subsequent items describe how the compensation signal is adapted to the changed f movement.

- After roughly 1 ms, the first or second green multiplier, depending on the sign of the f deviation, effects that the yellow integrator cannot continue to return towards zero (but still depart farther from zero).
- If the rampdown continues, that state lasts for 210 ms, and at the moment of its termination, the blue multiplier sets both limits of the dynamic saturation block to 0, i.e. the output value of the yellow integrator is frozen. This new state lasts until half the rampdown has passed.
- While that state is still active, the next state is already prepared (but not yet activated): After $1/4$ of the rampdown, when the rampdown value gets below 1.5, the third or fourth green multiplier, depending on the sign of the f deviation, ensures that the dynamic saturation block will still inhibit any further departure of the yellow integrator from zero as soon as its frozen state is released.
- After half of the rampdown has passed, the yellow integrator is no longer frozen but only regains the ability to return towards zero, see previous item. (It cannot pass through zero and take the other sign because that sign cannot pass through the yellow multiplier due to its upper input.) At the same time, another mechanism starts working (for the smooth realization of which the gain $-1/(0.7\text{ s})$ of the rampdown has been chosen):

After half of the rampdown has passed, the output values 1...0 of the blue integrator are used to cross-fade the raw value from which the compensation signal is calculated from the output of the blue sample&hold block to the output of the yellow integrator within 0.7 s.

- After the rampdown, the blue integrator remains at its minimum value of 0. Everything associated with the rampdown has been described under the premise that f remains more than 0.4 Hz above or below f_{rated} during the whole time. If, under the same premise, a new f departure should start in the same direction as before, no additional damping compensation will be provided but only what still comes from the output of the yellow integrator if it has not yet become zero. Such cases are possible but very unlikely, and the described behaviour preserves stability.
- As soon as f is back in the range ± 0.4 Hz around f_{rated} , the upper input of the OR block in front of the blue sample&hold block becomes TRUE, and the latter starts to follow the yellow integrator again. At the same time, the blue integrator goes back to its default state with an output value of 2.001. The damping compensation is prepared for a new f departure, be it of the same or the opposite sign.

The damping compensation subsystem can be removed from the VSM without replacement with no effect except that everything described here no longer works.

3 Systems

Two different AGI options are shown. One of them is DC-coupled and the other one is AC-Coupled.

3.1 DC AGI

The DC AGI connects PV, supercab, storage and load on the DC side. Detailed information is given in [6]. The overall structure is given in Figure 3.1.

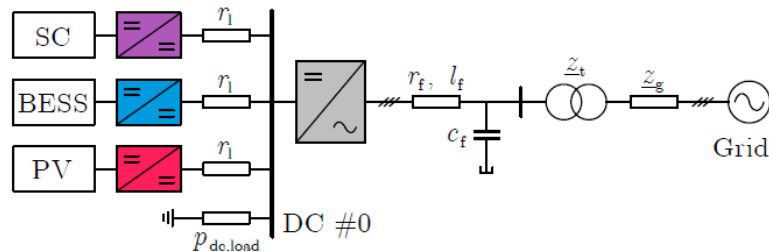


Figure 3.1: DC AGI [6]

The aggregated model [6] is also included in the Simulink model.

3.2 AC AGI

Following, the hydrogen production use case is shown, see deliverable D2.1. In this AC-coupled AGI, the battery delivers inertia in case of a frequency change. The use case is shown in Figure 3.2.

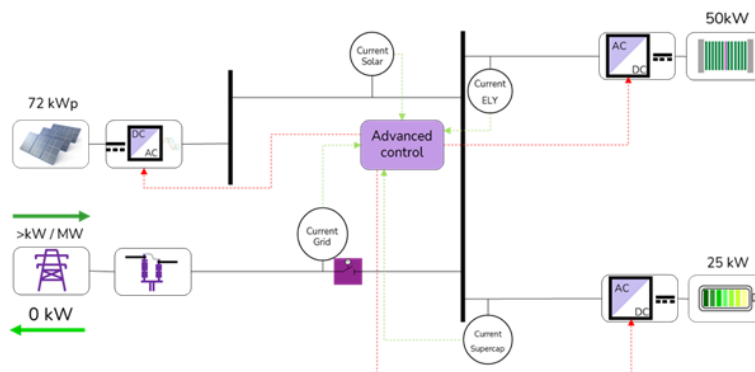


Figure 3.2: AC AGI - use case of one project partner



Bibliography

- [1] Stefan Boes, Bente Thamsen, Mattia Haas, Marianne Schmid Daners, Mirko Meboldt, and Marcus Granegger. Hydraulic characterization of implantable rotary blood pumps. *IEEE Transactions on Biomedical Engineering*, 66(6):1618–1627, June 2019.
- [2] Bin-Hao Chen, Po-Tuan Chen, Yen Liang Yeh, and Hua-Sheng Liao. Establishment of second-order equivalent circuit model for bidirectional voltage regulator converter: 48 v-aluminum-ion battery pack. *Energy Reports*, 9:2629–2637, 2023.
- [3] Daniel Duckwitz. *Power System Inertia: Derivation of Requirements and Comparison of Inertia Emulation Methods for Converter-Based Power Plants*. PhD thesis, Universität Kassel, 2019.
- [4] Daniel Duckwitz, Martin Shan, and Boris Fischer. Synchronous inertia control for wind turbines. In *2014 13th Wind Integration Workshop*. 2014.
- [5] Daniel Duckwitz, Friedrich Welck, and Christoph Glöckler. Operational behavior of the virtual synchronous machine. In *12. Fachtagung Netzregelung und Systemführung*. VDE Verlag, 2017.
- [6] Xiuqiang He, Josué Duarte, Verena Häberle, and Florian Dörfler. Grid-forming control of modular dynamic virtual power plants, 2024.
- [7] Marius Holst, Stefan Aschbrenner, Tom Smolinka, Christopher Voglstätter, and Gunter Grimm. *Cost Forecast for Low-Temperature Electrolysis - Technology Driven Bottom-Up Prognosis for PEM and Alkaline Water Electrolysis Systems*. Fraunhofer Institute for Solar Energy Systems ISE, 2021.
- [8] L. Lu and N. A. Cutululis. Virtual synchronous machine control for wind turbines: a review. *Journal of Physics: Conference Series*, 2019.
- [9] MATLAB. 400-kw grid-connected pv farm. https://de.mathworks.com/help/sps/ug/400-kw-grid-connected-pv-farm-average-model.html?s_tid=srchtitle_site_search_5_pv+converter, 2025. [Online; accessed 19-June-2025].
- [10] MATLAB. Capacitor. https://de.mathworks.com/help/simrf/ref/capacitor.html?searchHighlight=capacitor&s_tid=srchtitle_support_results_1_capacitor, 2025. [Online; accessed 19-June-2025].
- [11] MATLAB. Pv array. https://de.mathworks.com/help/sps/powersys/ref/pvarray.html?searchHighlight=solar+module&s_tid=srchtitle_support_results_6_solar+module, 2025. [Online; accessed 19-June-2025].
- [12] Cao-Khang Nguyen, Thai-Thanh Nguyen, Hyeong-Jun Yoo, and Hak-Man Kim. Improving transient response of power converter in a stand-alone microgrid using virtual synchronous generator. *Energies*, 11(1), 2018.
- [13] Christophe Nicolet. *Hydroacoustic modelling and numerical simulation of unsteady operation of hydroelectric systems*. PhD thesis, Lausanne, EPFL, 2007.



- [14] Chethan Parthasarathy, Hossein Hafezi, and Hannu Laaksonen. Lithium-ion bess integration for smart grid applications-ecm modelling approach. *IEEE Power & Energy Society Innovative Smart Grid Technologies Conference*, pages 1–5, 2020.
- [15] Yelun Peng and Xin Zhang. Analysis and improvement of transient load sharing between synchronous generator and virtual synchronous generator in islanded microgrid. In *2020 IEEE 9th International Power Electronics and Motion Control Conference (IPEMC2020-ECCE Asia)*, pages 1224–1228, 2020.
- [16] Xiangjun Quan, Xin Zhao, Liqi Zhang, Rong Xu, Yang Lei, and Alex Q. Huang. Novel power control of voltage-controlled inverters for grid inertia support. In *2019 IEEE Applied Power Electronics Conference and Exposition (APEC)*, pages 927–931, 2019.
- [17] Alain Sanchez-Ruiz and Matheus T. de Groot. High-power electrolyzer characterization via smart power converters. *International Journal of Hydrogen Energy*, 96:1243–1250, 2024.
- [18] Walter Schitteket_al. Complementary grid forming: Inertia gathered from constrained resources. *Submission on 9 July 2025 to IEEE Open Journal of Power and Energy*, preprint on <https://www.techrxiv.org/>, X(X), 2025.
- [19] Walter Schitteket_al. How to tailor power-electronic inertia to the constraints of its resource. *Submission on 9 July 2025 to IEEE Open Journal of Power and Energy*, preprint on <https://www.techrxiv.org/>, X(X), 2025.
- [20] J.-P. Thiran. Recursive digital filters with maximally flat group delay. *IEEE Transactions on Circuit Theory*, 18(6):659–664, 1971.
- [21] Peter Unruh, Maria Nuschke, Philipp Strauß, and Friedrich Welck. Overview on grid-forming inverter control methods. *Energies*, 13(10):2589, 2020.
- [22] VDE FNN. Technische anforderungen an netzbildende eigenschaften inklusive der bereitstellung von momentanreserve: Version 2.0.
- [23] Friedrich Welck, D. Duckwitz, and C. Gloeckler. Influence of virtual impedance on short circuit performance of virtual synchronous machines in the 9-bus system. In *NEIS 2017; Conference on Sustainable Energy Supply and Energy Storage Systems*, pages 1–7, 2017.
- [24] N. Wiese, Y. Zhang, and M. Braun. *New current limiting control for grid-forming converter under unbalanced faults*. IET Digital Library, 2022.
- [25] Nils Wiese, Daniel Duckwitz, Maria Nuschke, Yonggang Zhang, and Martin Braun. Fault operation of grid-forming converters with focus on system stability. In *11th Solar Integration Workshop*. 2021.
- [26] Low Wen Yao, J. A. Aziz, Pui Yee Kong, and N. R. N. Idris. Modeling of lithium-ion battery using matlab/simulink. In *IECON 2013 - 39th Annual Conference of the IEEE Industrial Electronics Society*, pages 1729–1734. IEEE, 2013.
- [27] Hui Zhang, Ruixue Zhang, Kai Sun, and Wei Feng. Performance improvement strategy for parallel-operated virtual synchronous generators in microgrids. *Journal of Power Electronics*, 19(2):580–590, 2019.
- [28] Lei Zhang, Xiaosong Hu, Zhenpo Wang, Fengchun Sun, and David G. Dorrell. A review of supercapacitor modeling, estimation, and applications: A control/management perspective. *Renewable and Sustainable Energy Reviews*, 81:1868–1878, 2018.
- [29] Hank Zumbahlen. The bess response: Mini tutorial mt-204.